nature nanotechnology

Article

https://doi.org/10.1038/s41565-025-02030-y

Low-iridium stabilized ruthenium oxide anode catalyst for durable proton-exchange membrane water electrolysis

Received: 17 November 2024

Accepted: 4 September 2025

Published online: 07 October 2025

Check for updates

Chang Qiu[1,10], Chase Sellers[1,10], Zhen-Yu Wu[1] ✉, David A. Cullen[2], Eli Stavitski[3], Akhil Tayal[3], Tae-Ung Wi[1], Mounika Kodali[4], Bryan Erb[4], Andrew Smeltz[4], Feng-Yang Chen[1], Yuge Feng[1], Zhou Yu[1], Ahmad Elgazzar[1], Tanguy Terlier[1,5], Thomas P. Senftle[1] ✉ & Haotian Wang[1,6,7,8,9] ✉

While mixing iridium (Ir) with ruthenium oxide (RuO_2) has proven to be an effective strategy for reducing Ir loading in anode catalysts for proton-exchange membrane (PEM) water electrolysers, achieving industrially relevant long-term stability typically requires an Ir-rich, Ru-lean combination. Here, by combining density functional theory with Metropolis Monte Carlo methods, we discovered that sufficient stabilization in the RuO_2 lattice could be achieved with less than 50 at.% of Ir, and that Ir in the first subsurface layer plays a critical role. By effectively dispersing Ir dopants within the RuO_2 lattice, we demonstrated an Ir:Ru atomic ratio of only 1:6 that exhibited exceptional stability for over 1,500 h of continuous water electrolysis at 2 A cm^{-2}. Our Ru_6IrO_x catalyst has the potential to reduce Ir loading by 80% compared with current commercial PEM water electrolysers, and its stability was further validated under industrial testing conditions in a 25-cm^2 PEM electrolyser.

Green hydrogen is playing a critical role in the global energy transition towards a low-carbon economy[1,2]. Among different green hydrogen production technologies, water electrolysis is widely considered as the most promising route to reach the scale of steam reforming at a competitive cost[3,4]. While alkaline water electrolysis currently dominates the market, proton-exchange membrane (PEM) water electrolysis has been gaining much momentum[5–7]. One major restriction of PEM water electrolysis is the use of iridium (Ir)-based catalysts at the anode due to the highly oxidative and acidic environment[8]. The price of Ir has reached as high as US$164 g^{-1} (ref. 9) and without reducing Ir usage, projected Ir demand in PEM water electrolyser alone can reach over 75% of the annual Ir production[10]. Given the extremely low production and high cost of Ir, the heavy reliance on Ir is becoming the most critical bottleneck for rapid expansion of PEM water electrolyser[11,12].

Finding an alternative to Ir has been a long-standing challenge. Ruthenium oxide (RuO_2)-based materials are widely regarded as the most promising candidates due to their high oxygen evolution reaction (OER) activity and a cost that is only one-tenth that of Ir[9]. However, they suffer from poor durability at elevated current densities[13,14]. The majority of RuO_2-based catalysts can be stably operated only under a few hundreds of milliamperes per square centimetre, which is well below the industrial requirement of ~2–3 A cm^{-2} (ref. 15). There have

[1]Department of Chemical and Biomolecular Engineering, Rice University, Houston, TX, USA. [2]Center for Nanophase Materials Sciences, Oak Ridge National Laboratory, Oak Ridge, TN, USA. [3]National Synchrotron Light Source II, Brookhaven National Laboratory, Upton, NY, USA. [4]De Nora Tech, LLC, Concord, OH, USA. [5]SIMS laboratory, Shared Equipment Authority, Rice University, Houston, TX, USA. [6]Department of Materials Science and NanoEngineering, Rice University, Houston, TX, USA. [7]Department of Chemistry, Rice University, Houston, TX, USA. [8]Rice Advanced Materials Institute, Rice University, Houston, TX, USA. [9]WaTER Institute, Rice University, Houston, TX, USA. [10]These authors contributed equally: Chang Qiu, Chase Sellers. ✉e-mail: wuzy@sustech.edu.cn; tsenftle@rice.edu; htwang@rice.edu

been attempts to fabricate Ru–Ir bimetallic oxide ($RuIrO_x$) with lower Ir contents[16–24]. Even though a few $RuIrO_x$ catalysts have been reported to deliver robust durability at industrial-level current density, the Ir content remains high at around 70 at.% (refs. 22–25). In addition, the stabilization mechanism of Ir in the RuO_2 lattice is less studied. This lack of understanding hinders the exploration of the lower limit of Ir content in RuO_2 required to achieve industrially relevant durability.

Here, we report a new lower limit of Ir loading required to stabilize the RuO_2 catalyst under industrial testing standards for PEM water electrolysis, as validated by an industrial partner. We used density functional theory (DFT) and a lattice-based Metropolis Monte Carlo (MMC) to understand the distribution of Ir in RuO_2 surface and subsurface regions and the effect of Ir on the vacancy formation of Ru. These simulations suggest that Ir predominantly resides in and stabilizes Ru from the subsurface, and that most Ru atoms in the RuO_2 surface can be stabilized with a relatively small amount of total Ir (<50 at.%.). Experimentally, by uniformly dispersing Ir dopants in RuO_2 lattice, we were able to reach a low Ir to Ru atomic ratio of 1:6 (Ru_6IrO_x) before signs of instability started to show. Under 2 A cm^{-2} in a PEM electrolyser, our Ru_6IrO_x catalyst demonstrated an outstanding stability of over 1,500 h without obvious signs of degradation. This stability was further confirmed by De Nora Tech in their 25-cm^2 PEM electrolyser while delivering a total water splitting current of 50 A. Our catalyst showed the potential to reduce Ir usage by more than 80% in both scenarios: when compared with standard commercial PEM water electrolysers and with a commercially available $RuIrO_x$ catalyst[25] (Supplementary Figs. 1 and 2 and Supplementary Table 1).

Theoretical evaluation of iridium–ruthenium stabilization

In general, the stability challenge of Ru is complex; several reasons have been suggested for the observed increase in Ru stabilization upon integrating certain metals into its oxide lattice[26]. There is experimental evidence that Ir plays a surface-mediated, rather than bulk-mediated, role in stabilizing the RuO_2 surface[27]. Ir is less prone to corrosion via demetallation, so this mechanism often invokes a 'shielding' effect wherein Ru atoms are blocked from direct exposure to the electrolyte by the more stable Ir atoms, thereby decreasing the possibility of OER-induced degradation. Whether the catalyst surface is enriched with Ir upon synthesis[27,28] or over time as a by-product of Ru leaching[29], Ir can stabilize Ru. However, the exact role Ir plays near the surface and how much Ir is required to stabilize RuO_2 during the OER remains unclear. As such, we applied DFT and Monte Carlo to obtain qualitative insight into three questions: (1) How does Ir, substitutionally doped in the lattice, affect the stability of Ru atoms at neighbouring lattice sites (if at all) and does this effect propagate to next-nearest neighbours? (2) Where does Ir preferentially integrate in the RuO_2 lattice? (3) Given the effects and preference observed in (1) and (2), is there a lower limit of Ir that could stabilize the entire RuO_2 surface?

We first sought to understand how an isolated Ir atom in the RuO_2 lattice affects the stability of neighbouring Ru atoms. Recent works on ruthenium-based materials have centred around Ru dissolution, wherein lattice Ru is oxidized as a by-product of the OER, dissolving as RuO_4 and eventually causing structural collapse of the RuO_2 lattice[30–32]. Metal vacancy formation has been identified as a reasonable descriptor for this process on the RuO_2(110) surface[31]. Ru dissolution results in the removal of a coordinatively unsaturated surface metal site (Ru_{CUS}) and (at least) its atop oxygen. To investigate how Ir affects the thermodynamic feasibility of Ru dissolution, here we calculate simple vacancy formation energies for removing Ru_{CUS} and its atop oxygen (Ru_{CUS}–O under several Ir-doping configurations, which we benchmark against the pristine, undoped surface (Supplementary Fig. 3). We began by simulating lattices containing a Ru_{CUS}–O vacancy at various distances from an isolated Ir atom substitutionally doped into one of each of four metal sites of RuO_2(110): coordinatively unsaturated site (CUS), bridge (BRI), and their first-subsurface counterparts, sub-CUS and sub-BRI (Fig. 1a and Supplementary Fig. 4). The nearest Ru_{CUS} neighbour of the Ir dopant in RuO_2(110) exhibited site-dependent shifts in Ru_{CUS}–O vacancy formation energy. When Ir occupied CUS and sub-BRI sites, the Ru vacancy-formation energy increased by 0.14 eV and 0.20 eV, respectively (Fig. 1b). By contrast, Ir at sub-CUS or BRI sites produced only negligible changes, which indicated that Ir in those sites at low concentrations would not influence Ru stability (Fig. 1b and Supplementary Table 2). Interactions between Ir and the second-nearest Ru_{CUS} neighbour also exhibited little change in the Ru vacancy formation energy for all site types compared with undoped RuO_2 (Supplementary Table 3). Thus, Ir stabilization is localized and site specific, driven by Ir on the surface (Ir_{CUS}) and in the subsurface layer ($Ir_{sub\text{-}BRI}$) (Supplementary Note 1).

We applied a MMC algorithm, driven by energetics derived from our DFT analysis, to understand the thermally equilibrated distribution of Ir atoms across metal sites in the RuO_2 lattice for a range of Ir concentrations (Supplementary Note 1). DFT-calculated energy differences between Ir- and Ru-occupied RuO_2(110) sites were directly input as swap energies in the MMC simulations (Supplementary Fig. 5). For bulk swaps, we assumed the same energy differences as subsurface swaps, an approximation validated by explicit tests on a larger surface model (Supplementary Fig. 6). Each MMC simulation assigned a specific Ir atomic fraction to a lattice model of a 4.1-nm particle, typical of our synthesized Ir-RuO_x nanoparticles, with sites designated as surface, first subsurface or bulk. For each run, a defined number of metal sites were populated with Ir atoms. The MMC algorithm then randomly selected an Ir-occupied site, proposed a swap with a randomly chosen Ru-occupied site and accepted or rejected the move using the Metropolis probability criterion based on the associated energy change. The process was repeated for $>10^6$ iterations after equilibrium to sample the thermally equilibrated Ir distribution (Supplementary Fig. 7 and Supplementary Note 2).

MMC simulations confirmed that Ir preferentially resides in subsurface and bulk sites. At low concentrations (<45 at.%), 12–19% of Ir atoms occupied sub-CUS sites and 38–30% occupied sub-BRI sites in the first subsurface layer. Around 48–50% resided in bulk CUS or BRI sites. Thus, less than 3% of Ir atoms remained in the surface layer after the MMC reached equilibrium (Fig. 1b, inset, and Supplementary Fig. 8). While the MMC simulations were parameterized with energetics from the RuO_2(110) facet, analogous calculations for other representative facets ((101) and (211)) confirmed similar preferences (Supplementary Figs. 9 and 10). The predominance of Ir beneath the surface at lower concentrations suggested two possibilities: if Ir can stabilize the entire surface (1) as the minority metal (that is, <50 at.% Ir), it does so from the subsurface; or (2) as the majority metal (that is, >50 at.% Ir) it is probably fulfilling a surface-mediated 'shielding' role. Given the promising nature of catalyst materials with minority Ir loadings, we aimed to answer an important question: can $Ir_{sub\text{-}BRI}$ alone support the stabilization of the entire RuO_2 surface?

We used the coordination numbers CNs between Ru_{CUS} and $Ir_{sub\text{-}BRI}$ from the simulated MMC models as a stability benchmark to identify the minimum loading needed to stabilize the entire RuO_2 surface. Particle size and the local coordination environment strongly influence the distribution of the Ir and, thus, its ability to stabilize the surface. Particle size defines the ratios between the number of surface, subsurface and bulk sites. As particle size increases, bulk site availability also increases, reducing the likelihood that Ir atoms distributed beneath the surface will occupy the first subsurface layer (Supplementary Note 3). In the case of the experimentally relevant 4.1-nm particle, this size resulted in the first subsurface layer composing much of the site availability beneath the surface (Supplementary Fig. 11). Moreover, for the (110) surface facet, one $Ir_{sub\text{-}BRI}$ can coordinate with up to two Ru_{CUS} in the lattice. Both of these factors resulted in a sharp increase in the probability of Ru_{CUS} coordination with $Ir_{sub\text{-}BRI}$ in the range of 0–40 at.% Ir.

https://doi.org/10.1038/s41565-025-02030-y

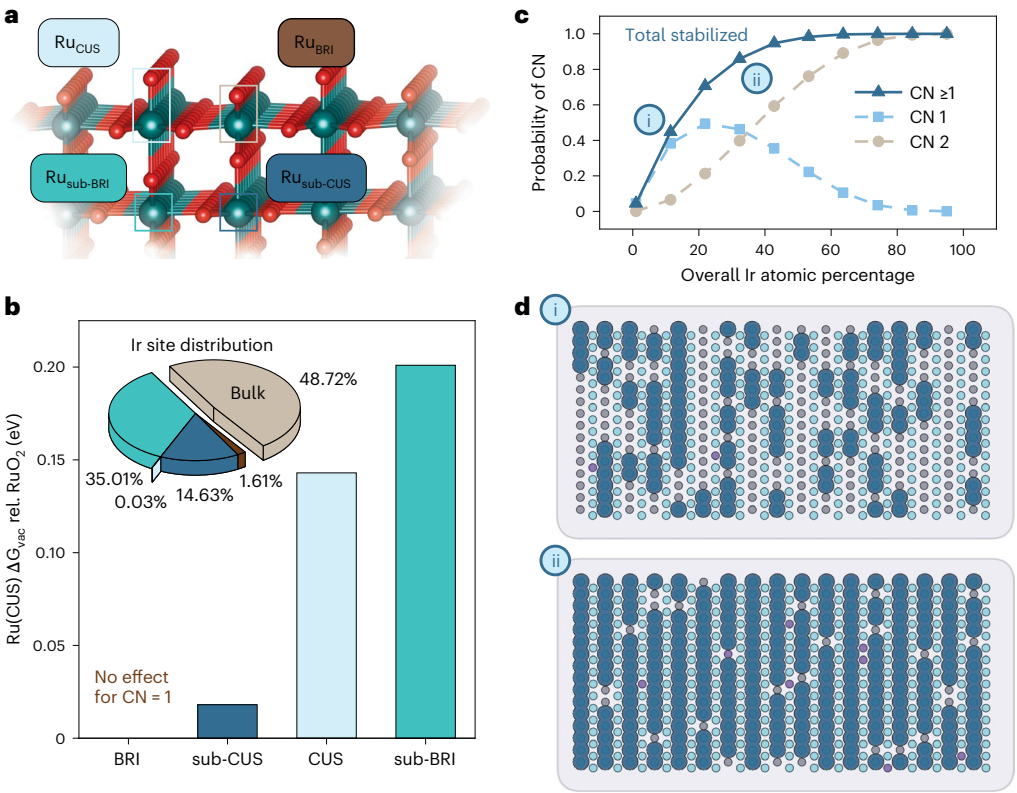

Fig. 1 | Computational assessment of Ir influence and distribution in RuO_2. **a**, RuO_2(110) lattice labelled with the metal site naming scheme where red and teal are oxygen and ruthenium atoms, respectively. **b**, The effect of an isolated Ir in RuO_2, located at different possible metal sites, on the energy required to remove the nearest ruthenium at a CUS site and its atop oxygen, computed relative (rel.) to pristine RuO_2(110). Inset: Ir distribution in the RuO_2(110) as computed by MMC at ~22 at.% overall Ir (among metal sites). **c**, Ru_{CUS} coordination number (CN) with subsurface Ir (Ir at the sub-BRI site) probability over a range of dopant concentrations computed by MMC. **d**, Top-down surface illustrations of the simulated lattices at (i) ~11 at.% iridium and (ii) ~ 32 at.% iridium (among metal sites) without depicting oxygen, where cyan denotes bridge (BRI) site Ru, purple denotes surface Ir and the grey atoms and blue heatmap represents CUS Ru atoms with a CN of zero or at least one with $Ir_{sub\text{-}BRI}$, respectively.

The majority of Ru_{CUS} were coordinated (that is, separated by only one oxygen) with at least one $Ir_{sub\text{-}BRI}$ as the sub-BRI sites were populated with Ir more favourably than others (Fig. 1c and Supplementary Table 4). This result suggests, qualitatively, that the majority of Ru_{CUS} could indeed be stabilized at Ir concentrations less than 50 at.% and that the stabilization at low Ir concentrations is driven by subsurface Ir, as illustrated in Fig. 1d. To explore the stabilization trend of Ru by Ir further, we performed synthesis, characterization and stability tests on RuO_2 nanoparticles with a range of Ir concentrations.

Catalyst synthesis and characterization

While our computational study suggested that it is possible to stabilize the RuO_2 lattice via a small fraction of Ir, the prerequisite is to ensure a uniform incorporation of Ir atoms. We adapted a two-step synthesis method to allow a more uniform distribution of Ir atoms inside the RuO_2 lattice[15] (Fig. 2a). Ir and Ru precursors of specified ratios were first adsorbed to the carbon black support under vigorous stirring, followed by annealing in H_2/Ar atmosphere at 800 °C. As shown in Fig. 2b, fine alloy particles of 1–3 nm were formed after annealing without evident phase segregation (Supplementary Fig. 12). This alloying intermediate step is to ensure a uniform mixture between Ru and Ir. The RuIr alloy on carbon was then calcined in air, during which the metals were oxidized and the carbon support was burnt away. The obtained material was then acid-leached to remove the unstable species before drying to yield the final product (Supplementary Note 4). To investigate the effects of Ir contents in Ir-RuO_x catalysts, we prepared three levels of concentration, including 14, 8 and 4 at.% of Ir, namely Ru_6IrO_x, $Ru_{12}IrO_x$ and $Ru_{24}IrO_x$. The Ir doping levels in the final products were in good agreement with those in the precursors, confirmed by both energy-dispersive spectrometry (EDS) and X-ray photoelectron spectroscopy (XPS) results (Supplementary Table 5). Constituting standardized synthetic steps, this synthesis method was readily adaptable to existing industrial reactor set-ups (Supplementary Table 6).

The XRD patterns of all synthesized catalysts (Fig. 2c) showed only characteristic peaks of rutile RuO_2 (Supplementary Note 5). High-angle annular dark-field scanning transmission electron microscopy (HAADF-STEM) images (Fig. 2d) confirmed the uniform size distribution of Ru_6IrO_x nanoparticles, with an average size of ~4.1 nm. More importantly, brighter atoms, which were not shown in STEM images of RuO_2 particles (Supplementary Fig. 13), were found to be scattered in Ru_6IrO_x (Fig. 1e,f), suggesting a homogeneous mixing of Ir in RuO_2. Clear lattice fringes were observed under a high magnification (Fig. 1f), suggesting a high-quality crystallinity of our Ru_6IrO_x catalyst. The uniform incorporation of Ir was further confirmed by EDS elemental mapping (Fig. 1g). The as-prepared $Ru_{12}IrO_x$ and $Ru_{24}IrO_x$ catalysts shared similar features to Ru_6IrO_x, such as particle size, high crystallinity and uniform Ir distribution (Supplementary Figs. 14 and 15). Simulations predicted an Ir-lean surface, although directly verifying surface–subsurface Ir differences remains highly challenging (Supplementary Note 6).

Electrochemical performance

To better understand the intrinsic characteristics of the Ir-RuO_x catalysts, OER activities of different as-prepared catalysts were evaluated in a rotating disk electrode (RDE) setup. According to the polarization curves (Fig. 3a), all Ir-RuO_x catalysts and the pristine RuO_2 showed similar OER activities, with overpotentials of ~240 mV to reach 10 mA cm^{-2}.

https://doi.org/10.1038/s41565-025-02030-y

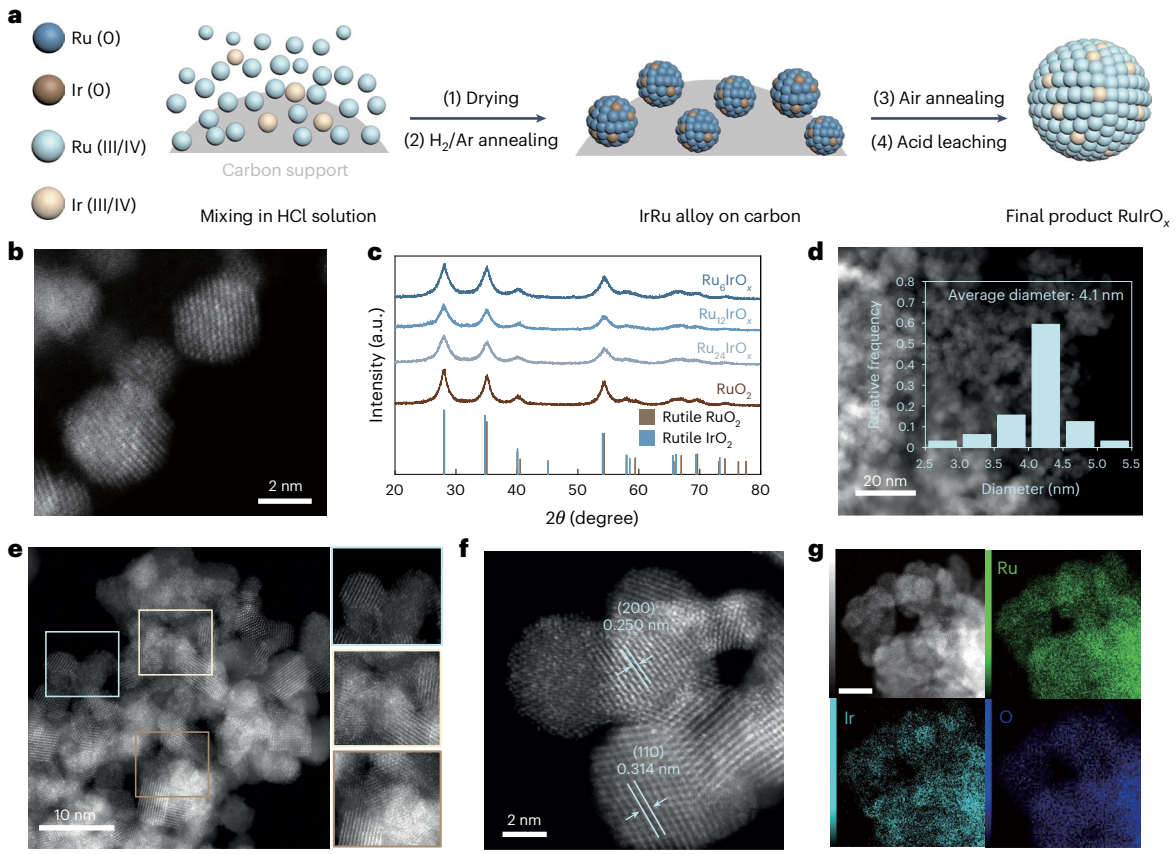

Fig. 2 | Synthesis and characterization of Ir-RuO$_x$. **a**, A schematic illustration of the catalyst synthesis method. **b**, A HAADF-STEM image of Ru_6Ir alloy on carbon support. **c**, XRD patterns of Ir-RuO$_x$ catalysts and RuO_2. **d**, A TEM image of Ru_6IrO_x. Inset: particle size distribution of Ru_6IrO_x. **e**, HAADF-STEM image of Ru_6IrO_x, with zoomed-in areas showing evidence of Ir incorporation. **f**, High-magnification HAADF-STEM image of Ru_6IrO_x. **g**, EDS elemental mapping of Ru_6IrO_x. Scale bar, 5 nm.

Their Tafel slopes were also comparable (Fig. 3b), suggesting minimal changes in the OER reaction mechanism after Ir incorporation (Supplementary Note 7). This similarity was also reflected in their electrochemical surface area (ECSA) (Supplementary Fig. 16 and Supplementary Table 7), as well as their ECSA-based polarization curves[17,19] (Supplementary Fig. 17).

To investigate the durability of our Ir-RuO$_x$ catalysts under industrially relevant operation conditions, we instead tested our catalysts in a PEM water electrolyser following industrial standards (Fig. 3c) (see more details in the Methods). It was encouraging to find that Ir-RuO$_x$ catalysts had similar polarization curves to that of RuO_2 (Supplementary Fig. 18), as RuO_2 is considered a more active species than IrO_2 (refs. 33,34). We fixed the water splitting current density at 2 A cm^{-2} during stability test (Fig. 3d), which is typically used in commercial PEM electrolysers[35,36]. Note that the relatively higher cell voltages observed in this figure, compared with commercial devices, can be attributed to room-temperature operation rather than high-temperature operation.

The stability curves showed a pronounced trend that the durability of Ir-RuO$_x$ was enhanced with higher levels of Ir incorporation, which agreed with our simulation results. The RuO_2 catalyst lost its OER activity under 2 A cm^{-2} in just tens of hours, consistent with previous reports that RuO_2 cannot stably sustain high current densities[15,37,38]. This rapid degradation was also evident in the dissolution tests (Fig. 3e), where RuO_2 exhibited a fast dissolution rate, highlighting its poor durability.

By contrast, a small fraction of Ir incorporation started to induce a notable improvement in operation durability. For example, the $Ru_{24}IrO_x$ catalyst maintained its cell voltage for over 200 h. However, its deficient stability was reflected in dissolution test results, as neither Ir nor Ru reached dissolution equilibrium during the test. The total Ir dissolution gradually reached as high as 4.5 μg mg_{Ir}^{-1} (Fig. 3f), albeit with Ru leaching out at a slower rate compared with RuO_2.

A major improvement was observed with $Ru_{12}IrO_x$, which showed voltage degradation ranging from 32 mV to 126 mV over 1,000 h. As suggested by the simulation results, if a catalyst has an Ir level near the threshold required to stabilize sufficient surface Ru atoms, its stability can become sensitive to subtle changes in Ir distribution. This sensitivity may explain the discrepancies in degradation rates observed between different batches of $Ru_{12}IrO_x$. An impressive suppression in dissolution was observed in $Ru_{12}IrO_x$, as both Ir and Ru dissolution readily reached equilibrium, which were 0.5 μg mg_{Ir}^{-1} and 20 μg mg_{Ru}^{-1}, respectively.

When Ir content was further increased to 14 at.%, the Ru_6IrO_x became stable enough to retain the potential though the 1,500-h test with minimal degradation rate of 2.3–2.8 μV h^{-1}. To provide a comprehensive evaluation of the durability, the stability tests were also carried out under constant voltage, in which Ru_6IrO_x maintained stable voltage over the testing period, while RuO_2 exhibited rapid deactivation (Supplementary Fig. 19). Given the supreme durability, it was not surprising that Ru dissolution plateaued at less than one-third the amount observed for $Ru_{12}IrO_x$, and Ir dissolution was barely detectable. This minimal dissolution, combined with the well-preserved structure and composition observed in the post-operation analysis (Supplementary Fig. 20 and Supplementary Table 8), demonstrated the superior structure durability and resistance of Ru_6IrO_x to the highly acidic and oxidative environment. Stable performance of Ru_3IrO_x and IrO_2 at 2 A cm^{-2} (Supplementary Figs. 21 and 22) further supports the stabilizing effect of higher Ir content.

https://doi.org/10.1038/s41565-025-02030-y

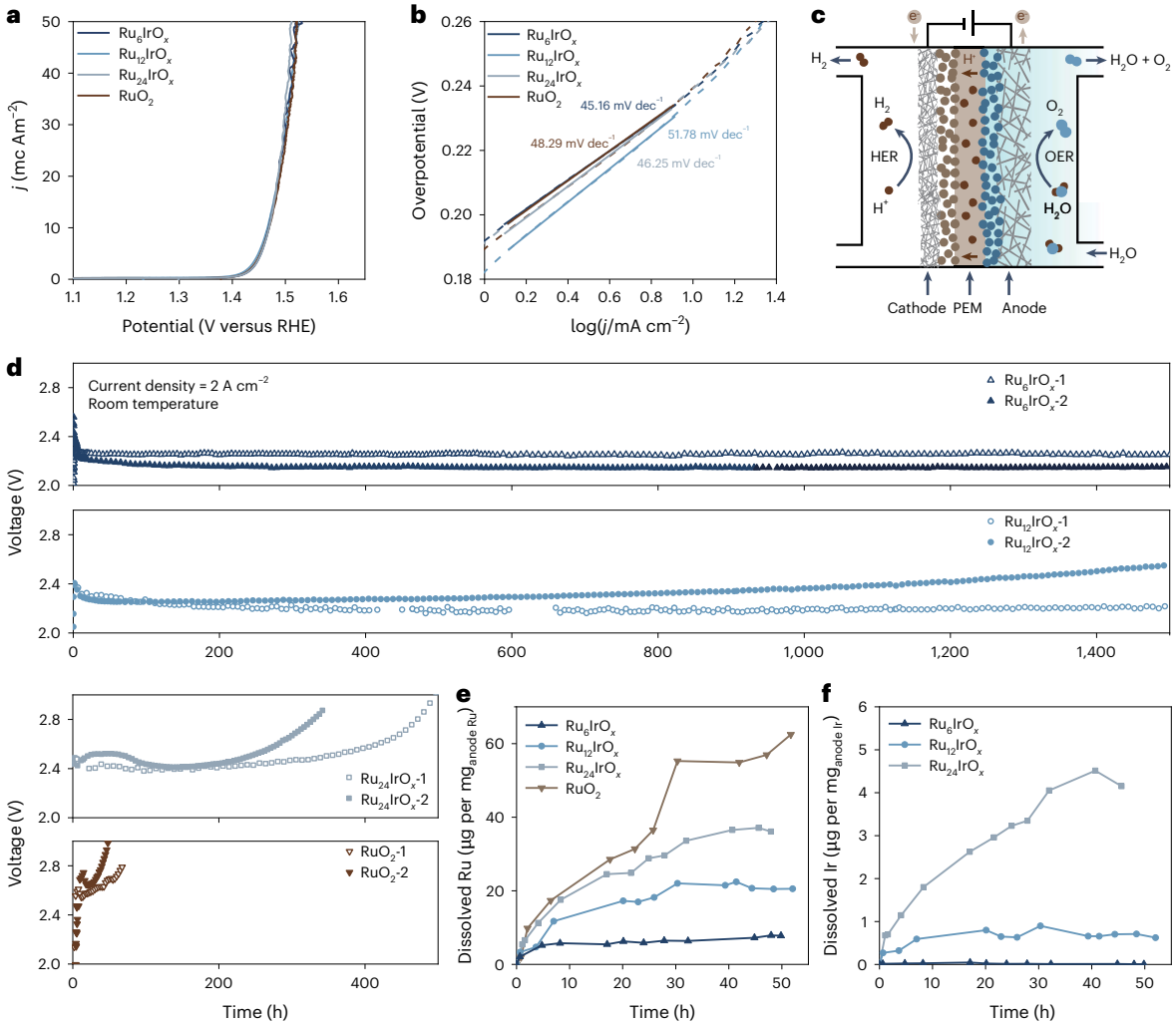

Fig. 3 | Electrochemical performance in an RDE and a laboratory-scale PEM water electrolyser. a, Polarization curves of Ir-RuO_x and RuO_2. **b**, Tafel plots of Ir-RuO_x and RuO_2. **c**, A schematic illustration of PEM water electrolysis. HER, hydrogen evolution reaction. **d**, Stability test results of Ir-RuO_x and RuO_2, all at 2 A cm^{-2} without iR correction. **e**,**f**, Dissolution test results of Ru (**e**) and Ir (**f**) of Ir-RuO_x and RuO_2, both normalized by corresponding anode metal loading.

To validate the outstanding durability of Ru_6IrO_x in a larger PEM electrolyser and under elevated temperature operation, our collaborators at De Nora Tech applied this catalyst to an anode in a 25-cm^2 PEM water electrolyser (Fig. 4a) following their standard testing protocols (Methods). Compared with commercial iridium black (IrB), Ru_6IrO_x demonstrated almost identical activity up to 1 A cm^{-2} (Fig. 4b), with slightly higher voltage above 1 A cm^{-2} despite having only one-third of the Ir. During the 1,600-h stability test (Fig. 4d), the current was gradually raised to 50 A and maintained at this level. The voltage initially rose from 1.939 V to 2.000 V in the first 500 h, probably indicative of a catalyst layer activation process. The voltage then experienced a slow decrease and reached 1.986 V when the test had to be stopped at 1,600 h due to other uses of the device. The superior durability of Ru_6IrO_x is also supported by the similar electrochemical impedance spectroscopy (EIS) curves of beginning and end of tests (Fig. 4c). Compared with other reported Ir-containing acidic OER catalysts (Supplementary Table 9), Ru_6IrO_x not only delivered stable performance at a high current density of 2 A cm^{-2} for over 1,500 h but also did so with dramatically lower Ir loading and weight percentage.

To demonstrate the economic advantage of our proposed catalyst, we conducted techno-economic analysis from multiple perspectives (Supplementary Note 8). First, even though the critical metal content in Ru_6IrO_x has not reached the long-term target (Supplementary Note 9), substituting our catalyst for IrO_2 reduces the anode catalyst cost by more than 80% compared with the United States Department of Energy (DOE) 2022 status[39], and also reduces the capital cost by US$82.1 per kilowatt. This substitution also greatly reduces the sensitivity of the Ru_6IrO_x catalyst's cost to Ir price volatility (Supplementary Note 10). Furthermore, compared with state-of-the-art earth-abundant OER catalysts, our catalyst can operate at much higher current densities[40–44], thereby allowing for smaller active area at a given hydrogen output and reducing the consumption of costly components.

In operando characterization of electronic structures

The catalysts of interest were examined using X-ray absorption spectroscopy (XAS) to investigate their electronic structure before, during and after catalysis (Supplementary Fig. 23). Compared with IrO_2, higher valence states and a reduction in *d*-band electrons of Ir were observed in Ru_6IrO_x, which were reported to enhance catalyst durability[45,46], as indicated by the white line shift of the Ir L_3-edge towards higher binding energy and the increased white line peak intensity in the X-ray absorption near-edge structure (XANES) spectra[47–49] (Fig. 5a). The bonding nature of Ir was further analysed using extended X-ray absorption fine structure (EXAFS) spectra (Fig. 5b). The Ru_6IrO_x catalyst

https://doi.org/10.1038/s41565-025-02030-y

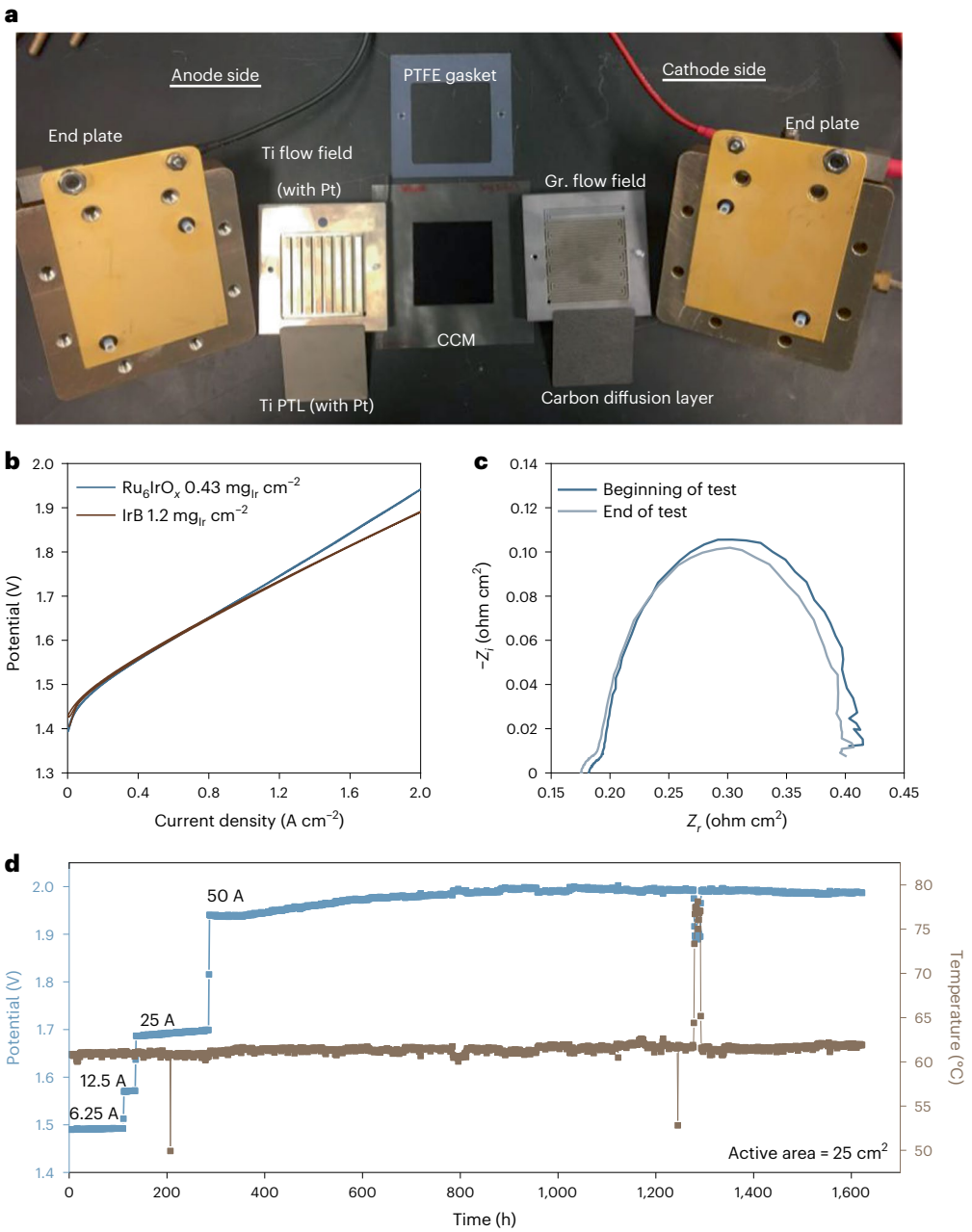

Fig. 4 | Validation of Ru_6IrO_x stability in De Nora's 25-cm² PEM electrolyser. a, Photo of electrochemical cell components used for scale-up tests. **b**, Polarization curves of Ru_6IrO_x and IrB at 60 °C. **c**, EIS plots of Ru_6IrO_x at the beginning and at the end of test. **d**, Stability test results of Ru_6IrO_x in a 25-cm² PEM water electrolyser with temperature control profile.

exhibited absence of a peak at 2.5 Å, implying the minimal presence of Ir–Ir bonding. Conversely, the strong peak at 1.6 Å can be attributed to Ir–O bonding that constituted the majority bonding of Ir in this catalyst. Besides, the second and third coordination shells of Ir in Ir-RuO_x shared similar features with Ru in RuO_2 (Supplementary Fig. 24), suggesting that Ir substitutes Ru in RuO_2 and adopts a similar coordination environment. Notably, a distinct peak at 3.4 Å appeared in the Ir L_3-edge EXAFS spectra of all Ir-RuO_x catalysts but was absent in the spectra of IrO_2 or Ir (Fig. 5b and Supplementary Fig. 25), which can be attributed to Ir–Ru scattering[50]. The Ir–Ru interaction was further corroborated by the wavelet transform (WT) of Ir L_3-edge EXAFS (Fig. 5g–i and Supplementary Fig. 26), as an enhanced signal can be observed at ~3.4 Å in all Ir-RuO_x catalysts[19,21]. A control sample of physically mixed IrO_2 (Supplementary Figs. 27 and 28) and RuO_2 of the same Ir content as Ru_6IrO_x rapidly lost activity within 20 h in PEM water electrolyser under 2 A cm^{-2} (Supplementary Fig. 29), underscoring the critical role of Ir–Ru interactions in enhanced durability.

Ru XAS results aligned closely with discoveries from that of Ir. The Ru K-edge position in Ru_6IrO_x XANES spectrum shifted towards lower binding energy[51] (Fig. 5c), suggesting that Ru accepts electrons from Ir (Supplementary Figs. 30 and 31), which was recognized as a sign of effective stabilization[52,53]. The Ru K-edge EXAFS spectra of Ir-RuO_x showed minimal deviation from that of RuO_2, with no obvious Ru–Ru scattering observed (Fig. 5d and Supplementary Fig. 32). This consistency was also reflected in their WT-EXAFS diagrams (Supplementary Fig. 33).

No obvious changes were observed during the in operando XAS measurements for both Ir L_3-edge and Ru K-edge of Ru_6IrO_x (Fig. 5e and Supplementary Fig. 34), even though the current density reached more than 400 mA cm^{-2} (Supplementary Fig. 35). Furthermore, minimal change in electronic structure was observed after PEM cell testing

https://doi.org/10.1038/s41565-025-02030-y

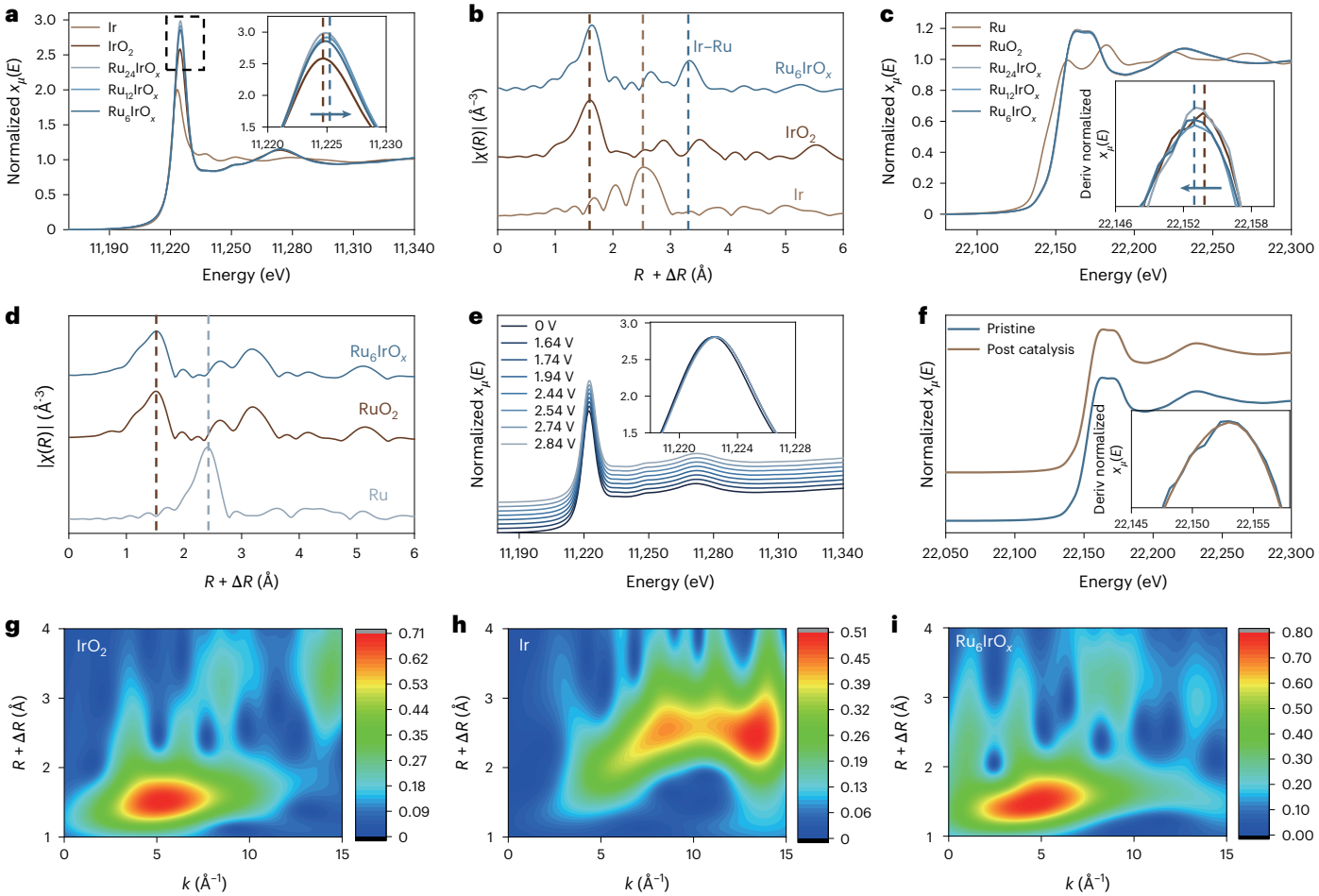

Fig. 5 | Electronic structure investigation by XAS. a, Ir L_3-edge XANES spectra of Ir-RuO_x, IrO_2 and Ir. Inset: magnified view of white line position. **b**, k^2-weighted Ir L_3-edge EXAFS spectra of Ru_6IrO_x, IrO_2 and Ir. **c**, Ru K-edge XANES spectra of Ir-RuO_x, RuO_2 and Ru. Inset: first derivation (Deriv) of Ru K-edge XANES spectra, the peak positions of which define edge positions. **d**, k^2-weighted Ru K-edge EXAFS spectra. **e**, In operando Ir L_3-edge XANES spectra of $Ru_{12}IrO_x$. Inset: magnified view of white line position. **f**, Ru K-edge XANES spectra of pristine and post-catalysis Ru_6IrO_x. Inset: first derivation of Ru K-edge XANES spectra. **g**–**i**, k^2-weighted Ir L_3-edge WT-EXAFS diagrams of IrO_2 (**g**), Ir (**h**) and Ru_6IrO_x (**i**). The white circle indicates an enhanced signal attributed to Ru–Ir scattering.

(Fig. 5f and Supplementary Figs. 36 and 37), consistent with the superior durability of Ru_6IrO_x.

Conclusion

In this study, we explored the lower limit of Ir incorporation level in RuO_2 lattice for durable PEM water electrolysis under industrially relevant operation conditions, coupling DFT and MMC methods. Ir incorporated in the first subsurface layer not only demonstrated the largest effect on stability, which was reflected by substantial increases in the vacancy formation energy of Ru_{CUS}, but was also the most favoured site under synthesis conditions. Our DFT and MMC computed results indicated that total surface stabilization could be achieved with less than 50 at.% Ir. By homogeneous mixing Ir into RuO_2 lattice, Ru_6IrO_x with 14 at.% Ir successfully sustained 2 A cm^{-2} for more than 1,500 h, the stability of which was further validated at total current of 50 A in a scaled-up cell by De Nora.

Our findings highlight that a lower Ir content without sacrificing stability could be attained with higher Ir concentration homogeneously distributed in the subsurface. While our computational results and post-mortem characterizations support this subsurface stabilization mechanism, direct tracking of subsurface Ir under long-term, industrially relevant conditions remains technically challenging, calling for future advances of in operando characterizations at atomic resolution. Besides, optimizing the synthesis procedure will be crucial to eventually achieving large-quantity production of consistent and high-quality catalysts. Moreover, greater attention should be given to industrial validation of electrochemistry publications claiming practical applications. These improvements will pave the way for next-generation low-Ir anode catalysts to replace IrO_2 as the dominant material in the PEM water electrolysis industry.

Online content

Any methods, additional references, Nature Portfolio reporting summaries, source data, extended data, supplementary information, acknowledgements, peer review information; details of author contributions and competing interests; and statements of data and code availability are available at https://doi.org/10.1038/s41565-025-02030-y.

References

1. Kovač, A., Paranos, M. & Marciuš, D. Hydrogen in energy transition: a review. *Int. J. Hydrog. Energy* **46**, 10016–10035 (2021).
2. Johnson, N. et al. Realistic roles for hydrogen in the future energy transition. *Nat. Rev. Clean. Technol.* **1**, 351–371 (2025).
3. Horri, B. A. & Ozcan, H. Green hydrogen production by water electrolysis: current status and challenges. *Curr. Opin. Green Sustain. Chem.* **47**, 100932 (2024).
4. Tüysüz, H. Alkaline water electrolysis for green hydrogen production. *Acc. Chem. Res.* **57**, 558–567 (2024).

5. Liu, R.-T. et al. Recent advances in proton exchange membrane water electrolysis. *Chem. Soc. Rev.* **52**, 5652–5683 (2023).
6. *IRENA Green Hydrogen Cost Reduction: Scaling up Electrolysers to Meet the 1.5 °C Climate Goal* (IRENA, 2020).
7. Chen, Y. et al. Key components and design strategy for a proton exchange membrane water electrolyzer. *Small Struct.* **4**, 2200130 (2023).
8. Wang, C. & Feng, L. Recent advances and perspectives of Ir-based anode catalysts in PEM water electrolysis. *Energy Adv.* **3**, 14–29 (2024).
9. PGM management. *Johnson Matthey* https://matthey.com/products-and-markets/pgms-and-circularity/pgm-management (2025).
10. Minke, C., Suermann, M., Bensmann, B. & Hanke-Rauschenbach, R. Is iridium demand a potential bottleneck in the realization of large-scale PEM water electrolysis?. *Int. J. Hydrog. Energy* **46**, 23581–23590 (2021).
11. Clapp, M., Zalitis, C. M. & Ryan, M. Perspectives on current and future iridium demand and iridium oxide catalysts for PEM water electrolysis. *Catal. Today* **420**, 114140 (2023).
12. Riedmayer, R., Paren, B. A., Schofield, L., Shao-Horn, Y. & Mallapragada, D. Proton exchange membrane electrolysis performance targets for achieving 2050 expansion goals constrained by iridium supply. *Energy Fuels* **37**, 8614–8623 (2023).
13. Wang, Q. et al. Long-term stability challenges and opportunities in acidic oxygen evolution electrocatalysis. *Angew. Chem.* **135**, e202216645 (2023).
14. Hou, L. et al. Strategies for the design of ruthenium-based electrocatalysts toward acidic oxygen evolution reaction. *EES Catal.* **1**, 619–644 (2023).
15. Wu, Z.-Y. et al. Non-iridium-based electrocatalyst for durable acidic oxygen evolution reaction in proton exchange membrane water electrolysis. *Nat. Mater.* **22**, 100–108 (2023.
16. Hrbek, T., Kúš, P., Kosto, Y., Rodríguez, M. G. & Matolínová, I. Magnetron-sputtered thin-film catalyst with low-Ir-Ru content for water electrolysis: long-term stability and degradation analysis. *J. Power Sources* **556**, 232375 (2023).
17. Cheng, J., Zhang, H., Chen, G. & Zhang, Y. Study of $Ir_xRu1–xO_2$ oxides as anodic electrocatalysts for solid polymer electrolyte water electrolysis. *Electrochim. Acta* **54**, 6250–6256 (2009).
18. Huynh, T. B. N. et al. Ir–Ru electrocatalysts embedded in N-doped carbon matrix for proton exchange membrane water electrolysis. *Adv. Funct. Mater.* **33**, 2301999 (2023).
19. Wen, Y. et al. Stabilizing highly active Ru sites by suppressing lattice oxygen participation in acidic water oxidation. *J. Am. Chem. Soc.* **143**, 6482–6490 (2021).
20. Joo, J. et al. Mn-dopant differentiating the Ru and Ir oxidation states in catalytic oxides toward durable oxygen evolution reaction in acidic electrolyte. *Small Methods* **6**, 2101236 (2022).
21. Zhu, W. et al. Stable and oxidative charged Ru enhance the acidic oxygen evolution reaction activity in two-dimensional ruthenium–iridium oxide. *Nat. Commun.* **14**, 5365 (2023).
22. Pantò, F., Siracusano, S., Briguglio, N. & Aricò, A. S. Durability of a recombination catalyst-based membrane-electrode assembly for electrolysis operation at high current density. *Appl. Energy* **279**, 115809 (2020).
23. Siracusano, S. et al. New insights into the stability of a high performance nanostructured catalyst for sustainable water electrolysis. *Nano Energy* **40**, 618–632 (2017).
24. Tao, L. et al. Mass-efficient catalyst layer of hierarchical sub-nanosheets on nanowire for practical proton exchange membrane electrolyzer. *Joule* **8**, 450–460 (2024).
25. Electrolyzer MEA - 3 Layer. *FUELCELL Store* https://www.fuelcellstore.com/electrolyzer-ccm (2025).
26. Chen, F.-Y., Wu, Z.-Y., Adler, Z. & Wang, H. Stability challenges of electrocatalytic oxygen evolution reaction: From mechanistic understanding to reactor design. *Joule* **5**, 1704–1731 (2021).
27. Escudero-Escribano, M. et al. Importance of surface IrO_x in stabilizing RuO_2 for oxygen evolution. *J. Phys. Chem. B* **122**, 947–955 (2018).
28. Kasian, O. et al. On the origin of the improved ruthenium stability in RuO_2–IrO_2 mixed oxides. *J. Electrochem. Soc.* **163**, F3099–F3104 (2016).
29. Escalera-López, D. et al. Phase- and surface composition-dependent electrochemical stability of ir-ru nanoparticles during oxygen evolution reaction. *ACS Catal.* **11**, 9300–9316 (2021).
30. Zagalskaya, A. & Alexandrov, V. Role of defects in the interplay between adsorbate evolving and lattice oxygen mechanisms of the oxygen evolution reaction in RuO_2 and IrO_2. *ACS Catal.* **10**, 3650–3657 (2020).
31. Klyukin, K., Zagalskaya, A. & Alexandrov, V. Role of dissolution intermediates in promoting oxygen evolution reaction at RuO_2(110) surface. *J. Phys. Chem. C* **123**, 22151–22157 (2019).
32. Cherevko, S. et al. Dissolution of noble metals during oxygen evolution in acidic media. *ChemCatChem* **6**, 2219–2223 (2014).
33. She, L. et al. On the durability of iridium-based electrocatalysts toward the oxygen evolution reaction under acid environment. *Adv. Funct. Mater.* **32**, 2108465 (2022).
34. Park, W. & Chung, D. Y. Activity–stability relationships in oxygen evolution reaction. *ACS Mater. Au* **5**, 1–10 (2025).
35. Kumar, S. S. & Lim, H. Recent advances in hydrogen production through proton exchange membrane water electrolysis—a review. *Sustain. Energy Fuels* **7**, 3560–3583 (2023).
36. Kuhnert, E., Hacker, V. & Bodner, M. A review of accelerated stress tests for enhancing MEA durability in PEM water electrolysis cells. *Int. J. Energy Res.* **2023**, 1–23 (2023).
37. Jin, H. et al. Dynamic rhenium dopant boosts ruthenium oxide for durable oxygen evolution. *Nat. Commun.* **14**, 354 (2023).
38. Sun, H. & Jung, W. Recent advances in doped ruthenium oxides as high-efficiency electrocatalysts for the oxygen evolution reaction. *J. Mater. Chem. A* **9**, 15506–15521 (2021).
39. Technical targets for proton exchange membrane electrolysis. *US Department of Energy* https://www.energy.gov/eere/fuelcells/technical-targets-proton-exchange-membrane-electrolysis (2022).
40. Kong, S. et al. Acid-stable manganese oxides for proton exchange membrane water electrolysis. *Nat. Catal.* **7**, 252–261 (2024).
41. Ram, R. et al. Water-hydroxide trapping in cobalt tungstate for proton exchange membrane water electrolysis. *Science* **384**, 1373–1380 (2024).
42. Chong, L. et al. La- and Mn-doped cobalt spinel oxygen evolution catalyst for proton exchange membrane electrolysis. *Science* **380**, 609–616 (2023).
43. Pan, S. et al. Efficient and stable noble-metal-free catalyst for acidic water oxidation. *Nat. Commun.* **13**, 2294 (2022).
44. Jo, S. et al. Nonprecious high-entropy chalcogenide glasses-based electrocatalysts for efficient and stable acidic oxygen evolution reaction in proton exchange membrane water electrolysis. *Adv. Energy Mater.* **13**, 2301420 (2023).
45. Li, A. et al. Atomically dispersed hexavalent iridium oxide from MnO_2 reduction for oxygen evolution catalysis. *Science* **384**, 666–670 (2024).
46. Flores, R. A. et al. Active learning accelerated discovery of stable iridium oxide polymorphs for the oxygen evolution reaction. *Chem. Mater.* **32**, 5854–5863 (2020).
47. Nong, H. N. et al. A unique oxygen ligand environment facilitates water oxidation in hole-doped $IrNiO_x$ core–shell electrocatalysts. *Nat. Catal.* **1**, 841–851 (2018).

48. Lee, W. H. et al. High crystallinity design of Ir-based catalysts drives catalytic reversibility for water electrolysis and fuel cells. *Nat. Commun.* **12**, 4271 (2021).
49. Shi, Z. et al. Confined Ir single sites with triggered lattice oxygen redox: toward boosted and sustained water oxidation catalysis. *Joule* **5**, 2164–2176 (2021).
50. Zheng, X. et al. Ir-Sn pair-site triggers key oxygen radical intermediate for efficient acidic water oxidation. *Sci. Adv.* **9**, eadi8025 (2023).
51. Wang, M. & Feng, Z. Pitfalls in X-ray absorption spectroscopy analysis and interpretation: a practical guide for general users. *Curr. Opin. Electrochem.* **30**, 100803 (2021).
52. Laha, S. et al. Ruthenium oxide nanosheets for enhanced oxygen evolution catalysis in acidic medium. *Adv. Energy Mater.* **9**, 1803795 (2019).
53. Liu, H. et al. Eliminating over-oxidation of ruthenium oxides by niobium for highly stable electrocatalytic oxygen evolution in acidic media. *Joule* **7**, 558–573 (2023).

Methods

DFT calculations

DFT calculations were carried out using the Vienna Ab Initio Simulation Package (VASP)[54,55] with the Perdew–Burke–Ernzerhof exchange-correlation functional[56]. Grimme's D3 dispersion correction was applied to account for long-range van der Waals interactions[57]. Projector augmented wave potentials[58] from the VASP library were used to describe the ionic cores of Ru, Ir and O atoms (explicitly treated valence electrons included Ru–$4d^7 5s^1$, Ir–$5d^8 6s^1$ and O–$2s^2 2p^4$). The plane-wave cut-off energy was set to 500 eV. The supercell dimensions of the RuO_2(110) and Ir-RuO_2(110) surfaces were constructed by repeating the unit cell six times along the *a*-axis and two times along the *b*-axis. For analysis of charge, oxygen adsorption, other surface facets or mechanistic data, different surface models are used (see the Supplementary Information for more details). The models included four layers RuO_2 stoichiometric layers with a vacuum gap of ~15 Å to prevent interactions between periodic images. Atop oxygens were added to CUS Ru sites in accordance with an ab initio analysis of synthesis conditions (Supplementary Fig. 38). Geometry optimizations were performed with a force convergence criterion of 0.02 eV $Å^{-1}$ and a self-consistent-field energy convergence criterion of 1×10^{-5} eV. For Brillouin zone sampling, a $2 \times 3 \times 1$ Monkhorst–Pack *k*-point grid was utilized for all slabs. All calculations were spin polarized. Further information on free energy calculations derived from VASP is provided in Supplementary Note 11. An ab initio molecular dynamics simulation of the most stable iridium-occupied site (Ir_{subBRI}) is also discussed in Supplementary Note 12.

MMC calculations

The MMC[59] simulations were lattice based with distinct lattice sites representing surface layer CUS and BRI sites, subsurface layer CUS and BRI sites, and bulk CUS and BRI sites. The number of each site type was approximated based on the geometric considerations of a spherical 4.1-nm-diameter Ir-RuO_2 nanoparticle, chosen to closely represent the average particle size synthesized experimentally (see Supplementary Fig. 11 and Supplementary Note 2 for detailed geometric approximations and model construction). The lattice was populated with either Ru or Ir atoms based on a random distribution with the number of each atom type determined by the user-specified Ir doping concentration. MMC sampling moves consisted of Ru–Ir position swaps. Acceptance or rejection of each proposed swap was governed by the Metropolis probability criterion, based explicitly on predefined energy differences calculated from the DFT energetics of corresponding atomic site swaps (using the slab models for Ir-RuO_2(110); Supplementary Fig. 5). For bulk-layer sites, energy changes were conservatively approximated as identical to subsurface-layer swaps, as explicit DFT tests confirmed negligible energetic differences between these site types (Supplementary Fig. 6). The temperature (*T*) was set to 773 K to represent catalyst synthesis conditions (see Supplementary Table 10 for all main MMC parameters).

Materials

$RuCl_3$, $IrCl_3 \cdot xH_2O$, NaOH, $HClO_4$, HCl and H_2SO_4 were purchased from Millipore Sigma. Isopropyl alcohol (IPA) was purchased from Honeywell. Polytetrafluoroethylene (PTFE) sheets were purchased from Grainger. Carbon black (BP2000) was purchased from CABOT, and 5% H_2 in Ar was purchased from Airgas. Platinized Ti felt, carbon papers with microporous layer (Sigracet 28BC), Fumasep FAS-50 membranes and Pt/C (20%) were purchased from Fuelcellstore. Nafion ionomer (D520CS) and Nafion 115 membrane were purchased from Chemours. All chemicals were used without further purification. Materials used at De Nora facilities are listed in the 'Electrochemical measurements at De Nora Tech facilities' section.

Catalyst synthesis

Ir-RuO_x catalyst synthesis. $RuCl_3$ and $IrCl_3 \cdot xH_2O$ were dissolved in 3 M HCl using a homogenizer (Branson). The total mass of Ir and Ru in precursors was 0.1 g. Then, 0.4 g carbon black was added to the solution, and the mixture was stirred for 12 h. After drying in a rotary evaporator (Heidolph), the obtained solids were further dried in oven for 12 h. The dried sample was first calcined in a tube furnace (Thermo Scientific) in 5% H_2/Ar atmosphere at 800 °C (ramping-up rate 10 °C min^{-1}) for 2 h, and after the furnace cooled down to room temperature, the obtained sample was further calcined in air at 500 °C (ramping-up rate 10 °C min^{-1}) for 4 h. After calcination, the powder was dispersed in 50 ml 1 M HCl and stirred overnight to perform acid leaching. The dispersion was then centrifuged and washed with water. The final product can be obtained after drying in an oven for 12 h.

RuO_2 and IrO_2 synthesis. RuO_2 and IrO_2 were synthesized following a similar procedure as Ir-RuO_x catalysts. To synthesize RuO_2, only $RuCl_3$ was mixed with carbon black in the first step. To synthesize IrO_2, only $IrCl_3 \cdot xH_2O$ was mixed with carbon black in the first step, and the oxidation temperature and time were changed to 800 °C (ramping-up rate 10 °C min^{-1}) and 5 h, respectively.

Characterization

TEM, HAADF-STEM images and EDS elemental mapping of $Ru_{24}IrO_x$ and RuIr alloy on carbon support were obtained using an FEI Titan Themis aberration-corrected transmission electron microscopy (TEM) at 300 kV. TEM, HAADF-STEM and EDS elemental mapping of Ru_6IrO_x, $Ru_{12}IrO_x$ and RuO_2 were acquired on a JEOL JEM-AMR200F 'NEOARM' equipped with an ASCOR probe corrector and operated at 200 kV. XPS data were measured on a ThermoFisher Nexsa G2 XPS using monochromatic Al Kα radiation (1,486.6 eV) and a flood gun as the neutralizer. XRD data were collected using a Rigaku Smartlab II diffractometer using Cu Kα radiation (wavelength 1.54056 Å), at scan speed of 10° min^{-1}. Ion concentrations were measured using PerkinElmer Nexion 2000B inductively coupled plasma mass spectrometry (ICP-MS).

XAS measurements were performed at the Inner Shell Spectroscopy beamline (8-ID)[60], National Synchrotron Light Source II, Brookhaven National Laboratory, using a Si(111) monochromator and a Passivated Implanted Planar Silicon detector. In operando tests were carried out using a homemade Teflon H cell filled with electrolyte of 1 M $HClO_4$; a Kapton-film-covered catalyst coated carbon paper working electrode served as the X-ray window for synchrotron radiation. Multistep potential control was used for the in operando measurements, with a hold time of ~20 min at each potential for the spectrum acquisition. XAS data processing was performed using Athena software. WT-EXAFS diagrams were generated using HAMA software, and Morlet wavelets were chosen to perform the transformation. Morlet wavelet parameters: $\kappa = 5$, $\sigma = 1$.

Electrochemical measurements using RDE

All three-electrode electrochemical measurements were performed using RDE equipment (Pine Instruments) at room temperature. To make the catalyst ink, 5 mg of catalyst and 20 µl 5% Nafion ionomer solution were dispersed in 1 ml IPA and sonicated in a bath sonicator (VWR) for 1 h. To coat the catalyst on glassy carbon electrode (5 mm in diameter), 16 µl of the ink was drop-cast on the electrode surface and vacuum dried, which resulted in catalyst loading of 0.4 mg cm^{-2}. The glassy carbon electrode was mounted onto the rotation rod of RDE and was used as working electrode, a saturated calomel electrode (SCE, CH Instruments) was used as the reference electrode and a carbon rod (Beantown Chemical) was used as the counter electrode. All electrodes were immersed in O_2-saturated 0.1 M $HClO_4$ electrolyte, and the rotation rate was kept at 1,600 rpm. All potentials were measured against the SCE and converted to potentials against reversible hydrogen electrode (RHE) using E (versus RHE) = E (versus SCE) + 0.241 V + 0.0591 × pH.

The pH of 0.1 M $HClO_4$ electrolyte used in this work was 1, which was determined by a pH meter (Orion Star A111, Thermo Scientific). The ohmic resistance arising from solution resistance and contact resistance was measured using potentiostatic EIS at frequencies ranging from 0.1 Hz to 200 kHz at 1.45 V versus RHE. All measured potentials in RDE are 100% iR compensated unless otherwise specified. The scan rate in LSV tests was 5 mV s^{-1}.

The ECSA was determined by

$$\mathrm{ECSA} = C_{\mathrm{dl}}/C_{\mathrm{s}}$$

where C_{dl} is the double-layer capacitance and C_{s} is the specific capacitance of sample. Here, C_{s} = 0.035 mF cm^{-2} was used based on reported values[15,61].

C_{dl} was determined by

$$C_{dl} = i_{\mathrm{c}}/\upsilon$$

where i_{c} is the charging current and υ is the scan rate. A series of cyclic voltammogram tests of different scan rates (2.5, 5.0, 7.5, 10 and 15 mV s^{-1}) were performed in the non-Faradaic potential region of 1.18–1.28 V versus RHE. By plotting the measured i_{c} versus υ, C_{dl} can be determined from the slope of the linear fitting.

Electrochemical measurements in PEM water electrolyser in laboratory

Before coating with catalyst, Nafion 115 membranes were first boiled in 5% H_2O_2 for 1 h. After cooling down and washing with deionized (DI) water, the membranes were boiled in 0.5 M H_2SO_4 for 1 h, followed by water washing and another 1 h boiling in water to ensure removal of impurities and full protonation. The obtained activated Nafion membranes were rinsed with DI water and stored in DI water for future use.

To coat anode catalyst onto membrane, an ink containing anode catalyst, Nafion ionomer and IPA was well mixed under sonication for 1 h and sprayed by an air spray gun onto a heated activated Nafion 115 membrane. The catalyst-coated membrane (CCM) was then boiled in 0.5 M H_2SO_4 for 1 h to be fully hydrated. To coat Pt/C (20%) onto carbon paper, an ink containing Pt/C, Nafion ionomer, water and IPA was well mixed under sonication for 1 h and sprayed onto a heated carbon paper with microporous layer. Anode catalyst loading was ~2 mg cm^{-2}, and Pt/C loading was ~0.6 mg cm^{-2}. The 2 mg cm^{-2} catalyst loading suggested the Ir mass loading of 0.38, 0.21 and 0.11 cm^{-2} in Ru_6IrO_x, $Ru_{12}IrO_x$ and $Ru_{24}IrO_x$, respectively. In both anode and cathode inks, the dry weight ratio of catalyst to Nafion ionomer was kept 5:1.

A customized titanium plate with flow field was used as the anode plate and a stainless-steel one was used as the cathode plate. To assemble the cell, a CCM was sandwiched between a platinized Ti felt and a catalyst-coated carbon paper. To test a commercially available $RuIrO_x$ CCM, an uncoated carbon paper was used as cathode electrode instead. Ti felt and carbon paper were fixed by PTFE sheets with a 1 cm × 1 cm window at the centre. The assembly was sandwiched by metal plates, and the torque applied was 2.8 Nm.

The voltages during PEM water electrolyser tests were recorded with a data logger (DATAQ DI-4108-E), and current was supplied by a power supply (Kungber). Room-temperature DI water was fed at the anode only at 0.4 ml min^{-1}. All PEM water electrolyser tests results are presented without iR correction. All post-catalysis CCM samples were tested in PEM water electrolyser for 80 h at 2 A cm^{-2}, unless otherwise specified.

Dissolution test

Dissolution tests were conducted in a three-chamber cell with 1-cm^2 active area to avoid deposition on cathode porous transport layer (PTL). A middle layer with a window at the centre is sandwiched between a catalyst coated Nafion 115 membrane and a Fumasep FAS-50 membrane. The assembly was then sandwiched between a platinized Ti felt and a catalyst-coated carbon paper, which were fixed by PTFE gaskets. The whole assembly was fixed between an anode Ti plate and a cathode stainless-steel plate.

The current was controlled at 1 A cm^{-2} for 50 h during the test. Anode, cathode and middle layer was fed with DI water, 1 M NaOH and 1 M $HClO_4$, respectively. All electrolytes were recycled to accumulate dissolved species and the total dissolution amount was summation of dissolved species in all electrolytes. Attempts have been made to operate at 2 A cm^{-2}, while the high current led to cell failure. We believe dissolution test at 1 A cm^{-2} was appropriate to reveal the trend of leaching amount among the catalysts of interest.

Anode samples of $Ru_{24}IrO_x$ and RuO_2 were diluted five times and then acidified to 0.2 M $HClO_4$, and middle layer samples of these two catalysts were also diluted five times. Anode samples of Ru_6IrO_x and $Ru_{12}IrO_x$ were acidified to 0.2 M $HClO_4$. All cathode samples were diluted 50 times to meet the requirement of total dissolved solids of ICP-MS. All samples tested using ICP-MS were calibrated with standards that had the same matrix. To be specific, standards diluted with 0.2 M $HClO_4$ were used for all anode samples and middle layer samples of $Ru_{24}IrO_x$ and RuO_2, those diluted with 1 M $HClO_4$ were used for middle layer samples of Ru_6IrO_x and $Ru_{12}IrO_x$, and those diluted with 0.02 M NaOH were used for all cathode samples. Additional explanations of the standard solution preparations and sample solution treatments are included in Supplementary Note 13.

Electrochemical measurements at De Nora Tech facilities

Ru_6IrO_x and 50 wt% Pt/C (Ames Goldsmith) were used as anode and cathode catalysts, respectively. Catalyst inks were prepared by ultrasonication in an ice bath for 30 min to achieve homogeneous dispersions. Catalysts inks contained the desired amount of the catalyst, 10 wt% Nafion ionomer, DI water and isopropanol (Sigma-Aldrich). The weight ratio of ionomer to catalyst was kept at 0.25 and an alcohol-to-water volume ratio of 3.

The CCM was fabricated using a combination of spraying coating and slot-die coating techniques. Following sonication, the anode catalyst ink was spray-coated onto a PTFE sheet at 30–35 °C while the cathode catalyst ink was coated onto a separate PTFE sheet using a slot-die coater. Both electrodes were then decal-transferred onto a Nafion 117 membrane through hot pressing. The final anode and cathode catalyst loadings were approximately ~2.3 mg_{cat} cm^{-2} and ~0.5 mg_{Pt} cm^{-2}, respectively with an effective area of 25 cm^2. IrB (TKK) was used as a reference anode catalyst. A CCM was prepared via similar protocol and IrB loading was ~1.5 mg cm^{-2} (1.2 mg_{Ir} cm^{-2}).

Platinized sintered titanium particle PTL (35-40% porosity, thickness 250 µm, De Nora) and Toray 090 carbon paper GDL (78% porosity, thickness 280 µm, Fuel Cell Store) were used as anode and cathode PTLs, respectively. A PTFE gasket with a thickness matching the PTL was used on the anode side. On the cathode side, a PTFE gasket 25% thinner than the carbon paper was used to achieve 25% compression of the carbon paper. A custom platinized parallel channel titanium flow field and a serpentine channelled graphite flow field (Fuel Cell Technologies) were used on the anode and cathode sides, respectively. The cell assembly was secured using metal endplates with a torque of 4.52 Nm.

The assembled cell was brought to 60 °C by pumping preheated DI water to the anode at a flow rate of 300 ml min^{-1}, and the electrical resistivity of the water was maintained above 2 MΩ cm^{-1} via an in-line mixed ion exchange column. No water was fed to the cathode. A current density of 0.25 A cm^{-2} was initially applied and then increased in a stepwise manner to reach 2 A cm^{-2}. At each current density step, the cell was held for few days to allow the voltage to stabilize before increasing the current density. After reaching 2 A cm^{-2}, linear polarization and EIS studies were conducted. Polarization studies were conducted by scanning the current from 0 to 50 A with a scan rate of 100 mA s^{-1}. EIS testing was conducted at 2.5 A with the frequency ranging from 20 kHz to 0.1 Hz to obtain the high-frequency resistance, with an amplitude of 0.1 A. Voltage stability was measured by holding current density

of 2 A cm^{-2} for 1,500 h, and the potential profile is presented without iR correction.

Data availability

The data that support the findings of this study are presented in the Article and its Supplementary Information. Extra data will be available from the corresponding authors upon reasonable request.

Code availability

All code used in this work central to its key findings is available via Github at https://github.com/tsenftle/OER.

References

54. Kresse, G. & Furthmüller, J. Efficient iterative schemes for ab initio total-energy calculations using a plane-wave basis set. *Phys. Rev. B* **54**, 11169–11186 (1996).
55. Kresse, G. & Furthmüller, J. Efficiency of ab-initio total energy calculations for metals and semiconductors using a plane-wave basis set. *Comput. Mater. Sci.* **6**, 15–50 (1996).
56. Perdew, J. P., Burke, K. & Ernzerhof, M. Generalized gradient approximation made simple. *Phys. Rev. Lett.* **77**, 3865–3868 (1996).
57. Grimme, S., Antony, J., Ehrlich, S. & Krieg, H. A consistent and accurate ab initio parametrization of density functional dispersion correction (DFT-D) for the 94 elements H–Pu. *J. Chem. Phys.* **132**, 154104 (2010).
58. Blöchl, P. E. Projector augmented-wave method. *Phys. Rev. B* **50**, 17953–17979 (1994).
59. Metropolis, N., Rosenbluth, A. W., Rosenbluth, M. N., Teller, A. H. & Teller, E. Equation of state calculations by fast computing machines. *J. Chem. Phys.* **21**, 1087–1092 (1953).
60. Leshchev, D. et al. The Inner Shell Spectroscopy beamline at NSLS-II: a facility for in situ and operando X-ray absorption spectroscopy for materials research. *J. Synchrotron Radiat.* **29**, 1095–1106 (2022).
61. Lin, Y. et al. Chromium–ruthenium oxide solid solution electrocatalyst for highly efficient oxygen evolution reaction in acidic media. *Nat. Commun.* **10**, 162 (2019).

Acknowledgements

This work was supported by the Robert A. Welch Foundation (grant no. C-2051-20230405), the the David and Lucile Packard Foundation (grant 2020-71371) and National Science Foundation (grant no. 2143941). Electron microscopy research was supported by the Center for Nanophase Materials Sciences (CNMS), which is a US Department of Energy, Office of Science User Facility at Oak Ridge National Laboratory. This research used the Inner Shell Spectroscopy (ISS, 8-ID) of the National Synchrotron Light Source II, a US Department of Energy (DOE) Office of Science User Facility operated for the DOE Office of Science by Brookhaven National Laboratory under contract no. DE-SC0012704. We acknowledge the use of the Shared Equipment Authority and Electron Microscopy Center at Rice University for their contributions to this research.

Author contributions

H.W. and T.P.S. supervised the project. Z.-Y.W. and C.Q. developed the catalyst synthesis method. C.S. performed the DFT and MMC simulations. D.A.C., T.-U.W., Y.F. and Z.Y. performed TEM characterizations. E.S., A.T. and C.S. performed XAS measurements. M.K., B.E. and A.S. performed PEM water electrolyser tests at De Nora Tech. T.T. assisted with the refinement of the ICP-MS methodology. C.Q. performed catalyst synthesis, characterizations, electrochemical tests and related data processing. C.S., A.E. and F.-Y.C. assisted with electrochemical tests. C.Q. and C.S. wrote the manuscript. H.W., T.P.S. and Z.-Y.W. revised the manuscript. All authors discussed the results and provided comments on the manuscript.

Competing interests

C.Q., Z.-Y.W. and H.W. are the inventors listed on a US patent application based on this study by Rice University. The other authors declare no competing interests.

Additional information

Supplementary information The online version contains supplementary material available at https://doi.org/10.1038/s41565-025-02030-y.

Correspondence and requests for materials should be addressed to Zhen-Yu Wu, Thomas P. Senftle or Haotian Wang.

Peer review information *Nature Nanotechnology* thanks Jongwoo Lim and the other, anonymous, reviewer(s) for their contribution to the peer review of this work.